

## Probing the role of grain boundaries in single Cu nanoparticle oxidation by *in situ* plasmonic scattering

Sara Nilsson <sup>1</sup>, Alvaro Posada-Borbón <sup>1,\*</sup>, Mario Zapata-Herrera <sup>2</sup>, Alice Bastos da Silva Fanta <sup>3</sup>, David Albinsson <sup>1</sup>, Joachim Fritzsche <sup>1</sup>, Vyacheslav M. Silkin,<sup>4,5,6</sup> Javier Aizpurua <sup>2,4</sup>, Henrik Grönbeck <sup>1</sup>, Ruben Esteban,<sup>2,4,†</sup> and Christoph Langhammer<sup>1,‡</sup>

<sup>1</sup>Department of Physics, Chalmers University of Technology, 412 96 Göteborg, Sweden

<sup>2</sup>Centro de Física de Materiales, Centro Mixto CSIC-UPV/EHU, P. Manuel de Lardizabal 5, 20018 San Sebastián/Donostia, Basque Country, Spain

<sup>3</sup>Center for Electron Nanoscopy, Technical University of Denmark, Fysikvej, 2800 Kgs Lyngby, Denmark

<sup>4</sup>Donostia International Physics Center, P. Manuel de Lardizabal 4, 20018 San Sebastián/Donostia, Basque Country, Spain

<sup>5</sup>IKERBASQUE, Basque Foundation for Science, 48009 Bilbao, Basque Country, Spain

<sup>6</sup>Departamento de Polímeros y Materiales Avanzados: Física, Química y Tecnología, Facultad de Ciencias Químicas, Universidad del País Vasco UPV/EHU, Apartado 1072, 20080 San Sebastián/Donostia, Basque Country, Spain



(Received 6 December 2021; accepted 11 March 2022; published 15 April 2022)

Grain boundaries determine physical properties of bulk materials including ductility, diffusivity, and electrical conductivity. However, the role of grain boundaries in nanostructures and nanoparticles is much less understood, despite the wide application of nanoparticles in nanophotonics, nanoelectronics, and heterogeneous catalysis. Here, we investigate the role of high-angle grain boundaries in the oxidation of Cu nanoparticles, using a combination of *in situ* single particle plasmonic nanoimaging and *postmortem* transmission electron microscopy image analysis, together with *ab initio* and classical electromagnetic calculations. We find an initial growth of a 5-nm-thick Cu<sub>2</sub>O shell on all nanoparticles, irrespective of different grain morphologies. This insensitivity of the Cu<sub>2</sub>O shell on the grain morphology is rationalized by extraction of Cu atoms from the metal lattice being the rate limiting step, as proposed by density functional theory calculations. Furthermore, we find that the change in optical scattering intensity measured from the individual particles can be deconvoluted into one contribution from the oxide layer growth and one contribution that is directly proportional to the grain boundary density. The latter contribution signals accumulation of Cu vacancies at the grain boundaries, which, as corroborated by calculations of the optical scattering, leads to increased absorption losses and thus a decrease of the scattering, thereby manifesting the role of grain boundaries as vacancy sinks and nuclei for Kirkendall void formation at a later stage of the oxidation process.

DOI: [10.1103/PhysRevMaterials.6.045201](https://doi.org/10.1103/PhysRevMaterials.6.045201)

### I. INTRODUCTION

The oxidation of metals has been a phenomenon of interest ever since the introduction of iron tools in approximately 3000 BC because oxidation is often connected with a deterioration of the surface or structural properties of metallic objects. With the advent of modern nanoscience and nanotechnology a new perspective on the topic has been introduced and the understanding of oxidation and corrosion processes at the nanoscale

has gained significant attention both from a fundamental and application perspective in areas like microelectronics [1], structural nanomaterials [2,3], and heterogeneous catalysis [4–7]. Focusing on metal nanoparticles, a key advance was the discovery of the nanoscale Kirkendall effect (NKE) in nanocrystals, which describes the formation of a cavity that is growing at the expense of the metallic core inside an oxide shell. The NKE, which first was observed for Co nanoparticles [8] and has since been demonstrated for Cu [9] and Ni [10] among others, is the consequence of faster metal ion outward diffusion through the oxide compared to oxygen ion inward diffusion. At the same time, for bulk or thin film polycrystalline systems, grain boundaries have been suggested to play an important role because the diffusion rate of Cu atoms along grain boundaries in nanocrystalline Cu has been found to be orders of magnitude higher than the diffusion within the lattice [11]. Specifically, at temperatures above 300 °C, higher oxidation rates for polycrystalline Cu films have been observed for systems with smaller grains and correspondingly larger abundance of grain boundaries, thereby highlighting their importance for Cu mass transport during oxidation at high temperature conditions [12,13].

\*Present address: Department of Chemical and Biological Engineering, University of Wisconsin-Madison, Madison, Wisconsin 53706, United States.

†ruben.esteban@ehu.eus

‡clangham@chalmers.se

Published by the American Physical Society under the terms of the [Creative Commons Attribution 4.0 International license](https://creativecommons.org/licenses/by/4.0/). Further distribution of this work must maintain attribution to the author(s) and the published article's title, journal citation, and DOI. Funded by [Bibsam](https://www.bibsam.com/).

For nanoparticles and nanostructures, however, similar investigations are lacking and the understanding of the role of morphological factors like grain boundaries on the oxidation mechanism and the optical (plasmonic) properties of such nanomaterials is poor. This is unfortunate because engineered nanoparticles and nanostructures, which are widely applied in nanoplasmonics and nano-optics [14], nanosensors [15–18], micro- and nanoelectronics [19,20], nanostructured battery electrodes [21], and as model systems in heterogeneous catalysis [22,23], are often created by processes involving nucleation and growth via evaporation or sputtering and are therefore often polycrystalline [19]. To this end, a recent transmission electron microscopy (TEM) study has revealed that grain morphology may significantly impact the oxidation mechanism by providing evidence that the presence of coherent twin boundaries suppresses the formation of Kirkendall voids in Cu nanowires [24]. At the same time, a generalization of these results to other types of nanoparticles and nanostructures is difficult due to additional structural factors of potential importance, such as differences in geometry and surface curvature, which are predicted to impact oxidation kinetics [25], as well as the presence of grain boundaries with larger misfit. Furthermore, while environmental TEM indeed enables the study of oxidation processes on metal nanoparticles *in situ* [26,27], it is inherently limited for monitoring only a handful of particles in each experiment, and beam damage can become a crucial problem. Specifically, the electron beam has been reported to both reduce Cu oxide [28] and lead to the deposition of a protecting carbonaceous layer [29], which dramatically slows down or even completely suppresses the oxidation process [30]. Therefore, both experimental and theoretical efforts are necessary to develop a conceptual mechanistic understanding of the role of the grain morphology in the oxidation of engineered metal nanoparticles and nanostructures.

In response, we have applied multiplexed plasmonic nanoimaging of single Cu nanoparticles with engineered grain morphologies to monitor their oxidation in 1% O<sub>2</sub> *in situ* at atmospheric pressure. To enable direct correlations between individual particle grain morphology and oxidation response, we have simultaneously applied *ex situ* TEM analysis of all the single nanoparticles imaged optically during oxidation. As the main results, we find (i) grain morphology independent growth of a Cu<sub>2</sub>O shell during the initial phase of oxidation, dictated by energetics in agreement with density functional theory (DFT) calculations of the rate limiting process and (ii) a strongly grain morphology dependent evolution of the optical response of the individual nanoparticles. Furthermore, from calculations on the effect of Cu vacancy accumulation on the optical scattering cross section we propose that the optical response reflects the accumulation of Cu vacancies in clusters at high-angle grain boundaries (HAGBs) during oxidation, which constitute the nuclei for Kirkendall void formation at a later stage of the oxidation process.

## II. RESULTS AND DISCUSSION

### A. Cu nanoparticle nanofabrication and structural characterization

We have nanofabricated arrays of 25 Cu nanoparticles with electron-beam lithography (EBL) onto TEM “windows”

with a 25-nm-thin SiN<sub>x</sub> membrane, which we made in-house following the recipe by Grant *et al.* [31]. Specifically, we nanofabricated multiple arrays of nanodisks with constant size within each array, with the particle sizes ranging from 85 to 145 nm in diameter and constant height of 40 nm. As a result of the particle nucleation and growth process during evaporation through the EBL mask, these particles are all highly polycrystalline directly after nanofabrication (examples in Fig. S1.1 of the Supplemental Material [32]). To fine-tune their state of polycrystallinity and obtain a range of morphologies that stretches from single crystals to polycrystals with up to 10 grains per particle within each array, we annealed the sample for 2 h at 400 °C in reducing 2% H<sub>2</sub> in Ar carrier gas (see the Methods section for details). For an initial structural characterization of the nanoparticle morphology obtained this way, we employed (high resolution) TEM imaging, selected area electron diffraction (SAED), and transmission Kikuchi diffraction (TKD) [Figs. 1(a)–1(f)]. The TKD analysis was performed on a set of 78 single nanoparticles with 100 nm nominal diameter to confirm the anticipated abundance of nanoparticle morphologies that include single crystals and polycrystals with HAGBs (Fig. 1(d)–1(f) and more examples in S1.4 [32]). Here, HAGBs are boundaries having a crystallite misorientation angle larger than 15°. We also note that we find only very few examples (less than 2%) of low-angle grain boundaries (LAGBs, with misorientation angle 2–15°) in the studied particles and that we therefore choose to ignore LAGBs in our further analysis. In a similar fashion we choose to omit the twin boundaries from further analysis, since their presence did not have a significant impact on the evolution of the single particle optical response during oxidation (details in Fig. S7.1 of the Supplemental Material [32]). Furthermore, coherent twin boundaries have previously been reported to not affect the oxidation rate and suppress Cu vacancy accumulation in Cu nanowires [24]. Comparing the total HAGB length derived from TKD and TEM image analysis, respectively, reveals both a significant abundance of particles without any HAGBs in our samples, and a good quantitative agreement between the two methods [HAGB length distribution in Fig. 1(g), twin grain boundary length and grain number distributions in Fig. S1.2-3 of the Supplemental Material [32]]. This is important because it turns out that TKD analysis leads to significant carbon contamination [29] that prevents the oxidation process in our experiments [33] (Sec. S2 of the Supplemental Material, carbon deposition from TKD in Fig. S2.1 [32]), whereas our specifically developed TEM imaging recipe does not affect subsequent oxidation (examples in Fig. S2.2-3 [32]), and we therefore, from here forward, rely only on TEM image analysis to characterize particle morphology and grain boundary structure to minimize carbon contamination effects.

### B. Multiplexed *in situ* single particle plasmonic nanoimaging of Cu nanoparticle oxidation

Using dark-field scattering spectroscopy of the localized surface plasmon resonance (LSPR) response, we have shown in an earlier study of individual *single crystalline* Cu nanoparticles that the change in their spectrally integrated scattering

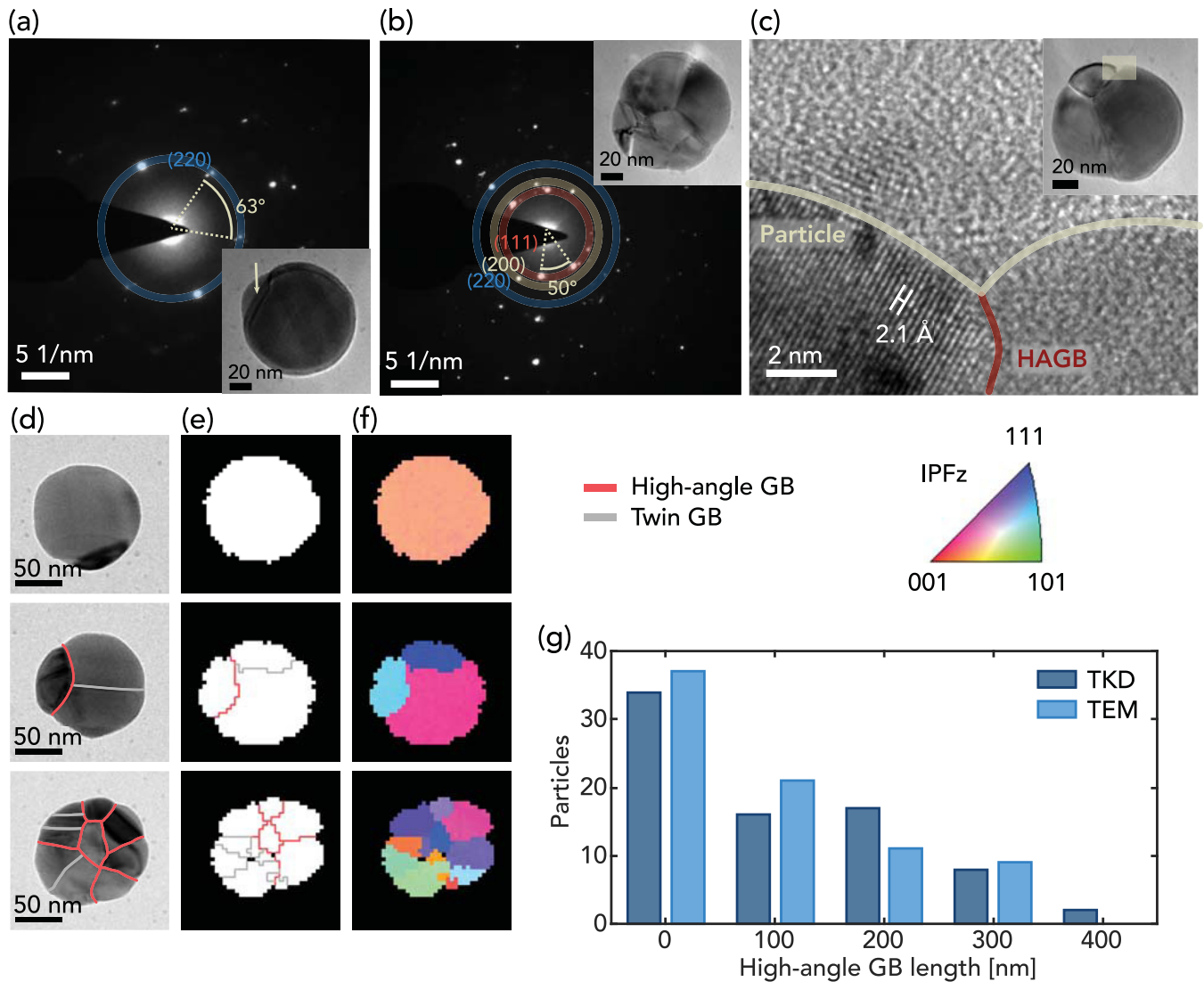


FIG. 1. Structural characterization of nanofabricated Cu particles. (a) SAED pattern of a 100-nm-diameter Cu nanoparticle with a twin boundary separating a large and a small grain (arrow in the inset TEM image of the particle), as indicated by the 63° angle between the corresponding diffraction points. (b) SAED of a 100-nm Cu particle with multiple HAGBs (see inset for TEM image) revealing a multitude of diffraction patterns that correspond to the individual crystallites with different lattice orientation. (c) High-resolution TEM image of a grain boundary (inset: overview image), where the lattice fringes of the left grain are clearly visible and with an indicated lattice spacing of 2.1 Å, corresponding to Cu(111). (d) TEM images representing the span of particle morphologies typically found in our samples, with likely twin boundaries and other HAGBs indicated with grey and red lines, respectively. Scale bars are 50 nm. Grain boundary (e) and crystallite orientation (f) maps obtained from TKD characterization of the same three particles. The crystallite orientations of the grains along the vertical direction are indicated according to the color-coding of the inverse pole figure (IPFz). (g) Distribution of HAGB length (excluding twin boundaries) obtained from a set of 78 single Cu particles by TKD analysis and TEM image analysis.

intensity,  $\Delta I$ , follows a specific pathway over time when they are oxidized to form  $\text{Cu}_2\text{O}$  [34]. Specifically, during the initial phase of the oxide formation process before the onset of Kirkendall void formation,  $\Delta I$  increases due to the growth of a homogeneous oxide shell around the metal core and the corresponding increase in refractive index (details in Fig. S3.1 [32]). In analogy, at identical conditions in terms of temperature and  $\text{O}_2$  partial pressure, we explore the role of HAGBs in the oxidation of individual *polycrystalline* Cu nanoparticles by employing multiplexed single-particle plasmonic nanoimaging [35]. Specifically, we apply it to simultaneously track the oxidation kinetics of large sets of individual particles

during the initial regime of oxidation, before the onset of Kirkendall void formation. For this purpose, we use a sample comprised of multiple arrays of 25 Cu nanoparticles with identical size nanofabricated onto a TEM window to enable TEM-based characterization of the particles both before and after the *in situ* plasmonic nanoimaging oxidation experiment. Within each array, the particles are spaced 4  $\mu\text{m}$  apart to ensure that they are resolved as individual point sources in the dark-field image used for the monitoring of their  $\Delta I$  optical response [Fig. 2(a)].

For the *in situ* oxidation experiment, we studied three particle arrays simultaneously, each containing 25 nanoparticles

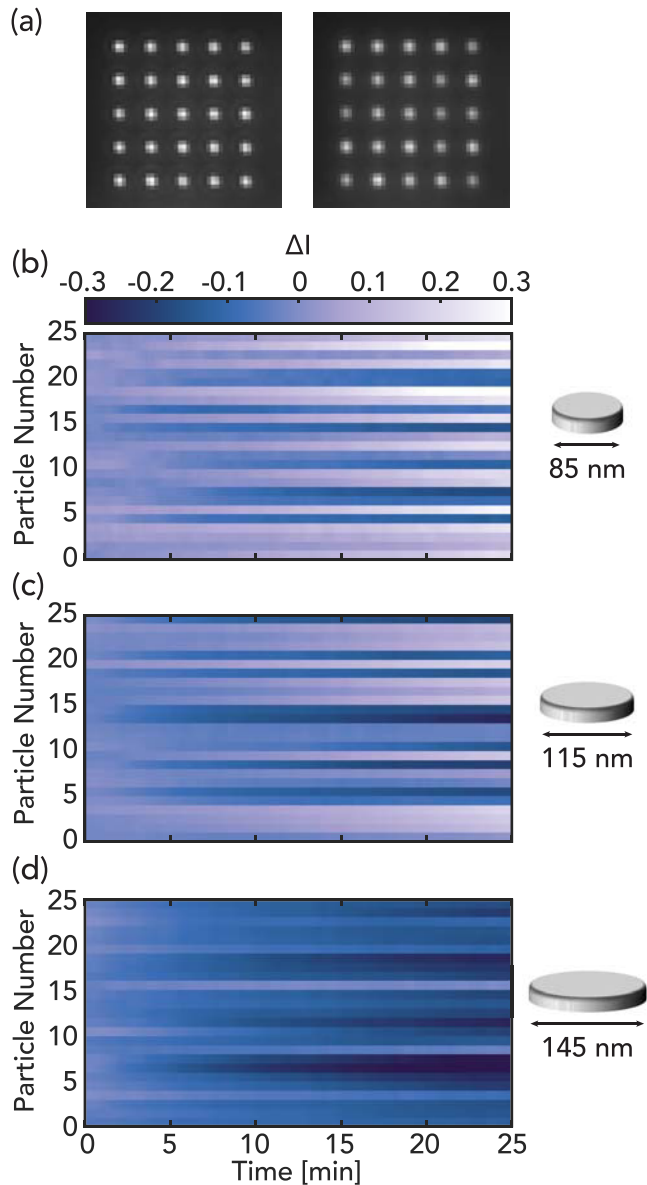


FIG. 2. *In situ* plasmonic nanoimaging readout of single Cu nanoparticle oxidation. (a) First and last dark-field scattering image taken at the start (left image) and end (right image) of 25-min exposure to 1% O<sub>2</sub> in Ar carrier gas at 150°C, picturing a 5 × 5 array of 115-nm Cu particles. The image is 24 × 24 μm and the distance between two particles is 4 μm. [(b)–(d)] Corresponding integrated scattering intensity change,  $\Delta I$ , time traces of 25 nanoparticles of each size, i.e.,  $D_0 = 85, 115,$  and 145 nm. Note that one subpopulation of particles exhibits an initially increasing  $\Delta I$  (light blue), whereas a second subpopulation exhibits a decreasing  $\Delta I$  (dark blue), and that the increasing intensity is found more often for the 85-nm particles.

of 85, 115, and 145 nm nominal diameter and a thickness of 40 nm (particle size histograms in Fig. S1.5 [32]). Prior to the oxidation experiment, the sample had been annealed for 2 h at 400°C in 2% H<sub>2</sub> in Ar carrier gas to induce a distribution of particle morphologies that ranges from single crystals to particles with up to 10 grains separated by HAGBs. To induce

oxidation, we then exposed the sample to 1% O<sub>2</sub> in Ar carrier gas at 150°C and extracted the  $\Delta I$  signal over time for each individual nanoparticle with diameter  $D_0 = 85$  nm [Fig. 2(b)], 115 nm [Fig. 2(c)], and 145 nm [Fig. 2(d)]. To obtain the optical scattering cross section, we collect the integrated scattering intensity from 400 to 900 nm and calculate the change in the scattering intensity with oxidation time  $\tau$  as  $\Delta I(\tau) = [I(\tau) - I_0]/I_0$ , where  $I_0 = I(\tau = 0)$ . As a first result, we find that the evolution of  $\Delta I$  is highly individual at the single particle level, with some particles indeed exhibiting the increase in  $\Delta I$  we have previously observed for single crystalline Cu nanoparticles [34] [brighter shade in Figs. 2(b)–2(d)], but also with a significant fraction of particles instead displaying a decrease in  $\Delta I$  [darker shade in Figs. 2(b)–2(d)]. Furthermore, it becomes evident that for the smallest studied particles ( $D_0 = 85$  nm), the largest fraction exhibits an increase in  $\Delta I$ , whereas for the largest studied particles ( $D_0 = 145$  nm) it is the opposite case, i.e., most particles exhibit a decrease in  $\Delta I$ . Accordingly, the intermediate size particles ( $D_0 = 115$  nm) exhibit both behaviors with about equal probability.

To identify the origin of this behavior, we recall that for single crystalline particles a positively increasing  $\Delta I$  is associated with the growth of a homogeneous Cu<sub>2</sub>O shell (details in Sec. S3 of the Supplemental Material [32] and Ref. [34]). It is therefore interesting to execute a *postmortem* TEM analysis of the formed oxide layers. TEM micrographs of three representative particles for each of the three sets of particle sizes [Fig. 3(a); for images of the same particles prior to oxidation see Fig. S4.1 [32]] and corresponding histograms of the effective oxide shell thickness,  $L_{\text{shell}}$ , derived from such images for all 25 particles of each size [Fig. 3(b)], reveal that the average  $L_{\text{shell}} = 4.9 \pm 0.5, 4.8 \pm 0.4,$  and  $5.1 \pm 0.4$  nm for the  $D_0 = 85-, 115-,$  and 145-nm particles, respectively. We thus neither identify a significant difference in the thickness of the formed oxide layer for the different particle sizes nor an obvious correlation between the grain structure and the formed oxide layer thickness (for oxide shell thickness vs HAGB density of individual particles see Fig. S4.2 [32]). There is no oxide thickness difference despite a significantly higher abundance of single crystals in the 85-nm particle set compared to the 115- and 145-nm ones [HAGB density in Fig. 3(c) and crystal grain numbers in Fig. S1.6], and despite the distinctly different  $\Delta I$  response observed between individuals and across the three sets of particle size (cf. Fig. 2). This indifference of the oxide thickness has two important intermediate consequences. (i) The rate of oxide shell growth is independent from the abundance of HAGBs and independent from particle size, since oxide shells with essentially identical thickness are formed, in good agreement with a Cabrera-Mott oxidation mechanism [25,36,37] and corresponding observations for polycrystalline thin films, for which granularity was found to impact oxidation rates only for temperatures above 300°C [13] and after 20 nm oxide growth [36]. (ii) The  $\Delta I$  response, in contrast, indeed correlates with the abundance of HAGBs since the largest fraction of particles that exhibit a  $\Delta I$  increase during oxide shell formation are to be found in the set with 85 nm diameter, where single crystals are most abundant [Figs. 2(b) and 3(c)].

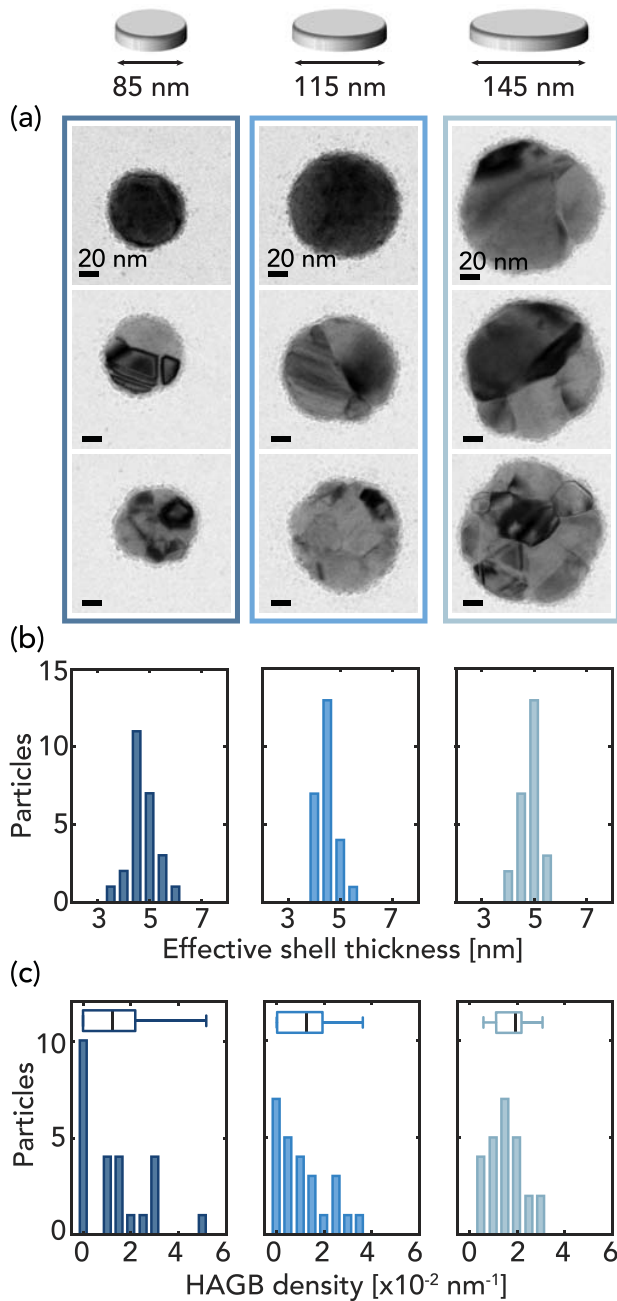


FIG. 3. Oxide shell thickness distribution. (a) Representative TEM images for three particles of each size after 25 min oxidation. The selected particles represent single crystals without HAGBs for 85 and 115 nm, a particle with two grains for 145 nm (top row), and particles with intermediate (middle row) and high (bottom row) HAGB densities. All scale bars are 20 nm. (b) Distributions of effective oxide shell thicknesses in the three particle size populations, yielding average shell thicknesses,  $L_{\text{shell}}$ , of  $4.9 \pm 0.5$ ,  $4.8 \pm 0.4$ , and  $5.1 \pm 0.4$  nm for the 85-, 110-, and 145-nm size particles, respectively. (c) HAGB density distribution for the three particle size populations obtained by normalizing the determined HAGB length with the projected particle area. The black lines in the box plot insets at the top of each histogram are the median values of each particle size, which are  $0.012$ ,  $0.012$ , and  $0.019 \text{ nm}^{-1}$ , for the particle sizes 85, 115, and 145 nm, respectively. Note the higher median HAGB density and the complete absence of single crystals for the 145-nm particle set.

### C. Density functional theory calculations of the Cu oxidation energy landscape

To elucidate the potential effect of grain boundaries on oxide growth, it is important to establish which processes are associated with high energy barriers. To this end, the growth of an oxide film can be limited either by the creation of vacancies in the metal phase or the diffusion of Cu ions in the metal or the oxide phase. Therefore, we study the energy landscape by DFT calculations of representative terrace and step structures (details in Sec. S5 of the Supplemental Material [32]). First of all, the initial oxidation of Cu surfaces is facile with the formation of numerous different structures [38,39]. For the continued oxide growth, we investigate the energy landscapes of Cu adatom extraction and diffusion on a terrace and step surface [Figs. 4(a) and 4(b)]. The extraction of an adatom on a Cu(100) terrace is associated with a barrier of 1.65 eV, and the following diffusion of the adatom over the metal surface is facile [Fig. 4(b)]. In comparison, extracting Cu adatoms from the step edge is associated with a lower barrier than from the terrace, thanks to the undercoordination of the Cu(911) surface. However, the diffusion barrier is similar on both surfaces [Fig. 4(b)]. Furthermore, there is a strong energy gain by incorporating the metal atom in the  $\text{Cu}_2\text{O}$  oxide from both surfaces, which motivates Cu adatoms jumping from the metal surface to the oxide phase.

Next, we focus on the barriers for Cu atom or vacancy diffusion in the metal and  $\text{Cu}_2\text{O}$  oxide lattice, which are of importance for the supply of Cu atoms for continued oxide growth. However, the formation of Cu interstitials in Cu and  $\text{Cu}_2\text{O}$  is highly endothermic [40], which motivates Cu vacancy diffusion as the relevant pathway. We have calculated the barrier for vacancy diffusion in fcc Cu to be 0.73 eV. In the oxide, the diffusing Cu cation finds a local energy minimum between the two bulk positions [split vacancy in Figs. 4(c) and 4(d)] with a diffusion barrier of 0.29 eV (in accordance with Ref. [41]).

From these DFT results, we conclude that the barriers for extraction of Cu adatoms from the terrace or step are clearly higher than the barriers associated with vacancy diffusion in either the metal or the oxide. Thus, the calculations suggest that extraction of Cu atoms from the metal phase is kinetically limiting the oxide growth. This scenario is consistent with the experimental observation that grain boundaries do not strongly affect the oxide film growth rate.

### D. Understanding the impact of HAGBs on the optical response $\Delta I$

Having established the energetic reasons for the experimentally observed independence of the oxide layer growth rate from the abundance of HAGBs in the nanoparticles across all three considered particle sizes, we now turn to discuss the origin of the observed single particle specific optical  $\Delta I$  response and its dependence on particle grain morphology. As the first step, we have performed electromagnetic simulations of the optical scattering cross section of a Cu nanodisk using COMSOL Multiphysics [42], with increasing nanoparticle diameter  $D_0 = 80, 100, 120, 140,$  and  $160$  nm and constant thickness of 40 nm. We increased the oxide shell thickness

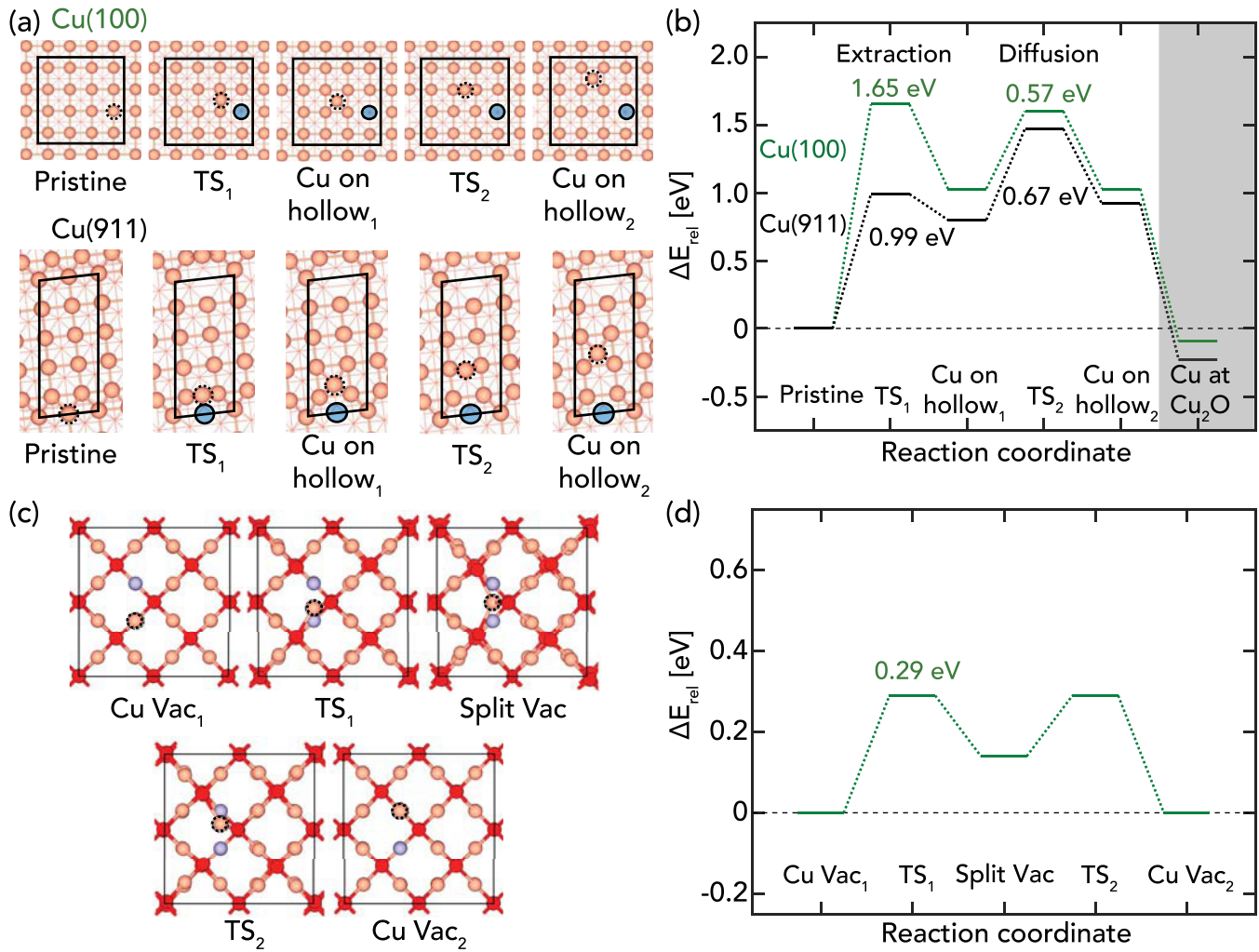


FIG. 4. Energy landscape of Cu atom extraction and Cu<sub>2</sub>O formation. (a) The formation of a Cu vacancy (blue)–adatom (dashed circle) pair together with the diffusion of the Cu adatom are visualized for Cu(100) terrace (top row) and Cu(911) step (bottom row). (b) A comparison of the energy landscape of the equilibrium and transition states (TSs) in (a) for extracting a Cu atom from Cu(100) (green line) and from a Cu(911) step (black line). In both cases a higher barrier for Cu atom extraction compared to adatom diffusion is observed. (c) Structures for Cu vacancy diffusion in Cu<sub>2</sub>O via a split-vacancy configuration, with the same color-coding as in (a): Cu (pink), O (red), and empty lattice sites (blue). (d) Energy landscape for Cu vacancy diffusion in Cu<sub>2</sub>O via a split-vacancy configuration as illustrated in (c).

systematically from 0 to 5 nm in 1-nm steps for each nanoparticle diameter. The shell was simulated as Cu<sub>2</sub>O, which we identified as the dominating oxide using high resolution scanning transmission electron microscopy (STEM) (Fig. S6.1 [32]), and which also previously has been observed to form at similar oxidation temperature and pressure [43–45]. As the main results from these simulations, we find that  $\Delta I$  increases linearly with the oxide shell thickness for all considered particle diameters [34] and that the  $\Delta I$  magnitude compared to the pristine Cu nanodisk is largest for the smallest disk diameter [Fig. 5(a)]. The latter can be understood on the basis that the same oxide shell thickness will provide a larger relative change to the particle morphology, and hence, the relative  $\Delta I$  will be larger for the smaller disks that are starting out with a smaller optical scattering cross section.

As the next step, focusing first only on the  $D_0 = 85$ -nm particles due to the largest number of single crystals in this set, we plot the experimental  $\Delta I$  time traces of all 25 individuals

measured simultaneously [Fig. 5(b)] by grouping them into single crystals and polycrystals. This analysis reveals that all single crystals indeed follow the simulated positive  $\Delta I$  change over time as the oxide grows, whereas the polycrystals do so to a lesser degree or not at all. This becomes even more apparent when plotting the  $\Delta I$  value obtained after completion of the 25-min oxidation as a function of HAGB density, which reveals a direct correlation between the magnitude of  $\Delta I$  and the HAGB density [85-nm particles in Fig. 5(c), equivalent analysis for 115 and 145 nm particles in Fig. S7.2 [32]].

To further investigate the observed trends, we develop a model to discriminate different contributions to the total  $\Delta I$  response obtained for the individual particles. Specifically, we fit the Johnson-Mehl-Avrami-Kolmogorov (JMAK) model [46,47] to the ten single crystal  $\Delta I$  traces in the 85-nm particle data set [thick gray line in Fig. 5(b)], to thereby extract the shell-growth contribution to the intensity change,  $\Delta I_{\text{shell}}$ . Here, we speculate that the increasing oxide growth rate ob-

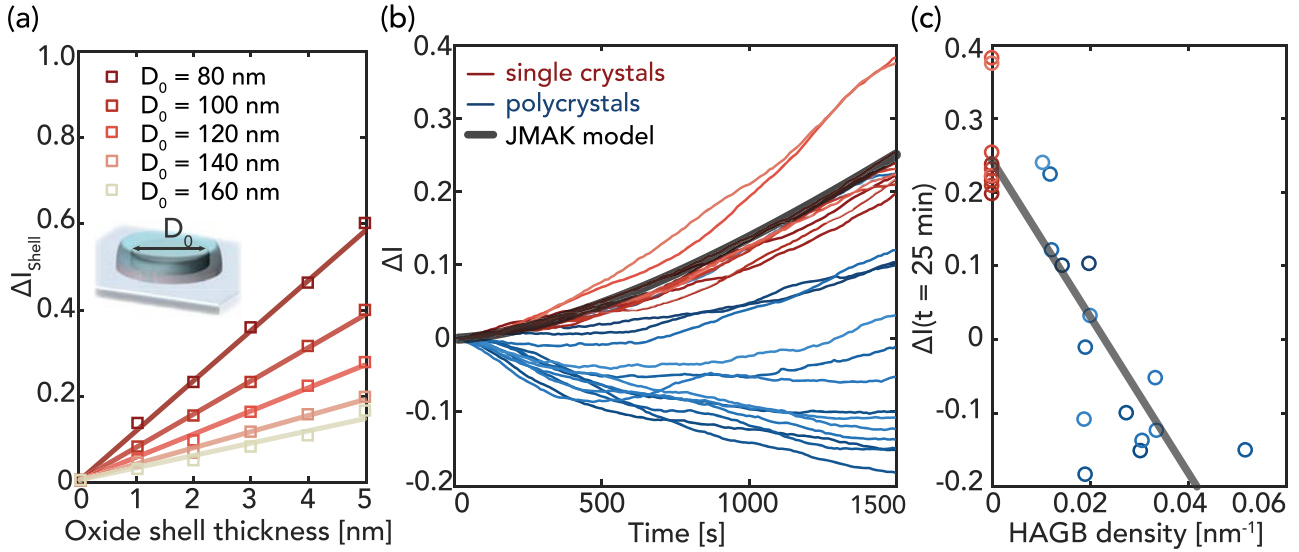


FIG. 5. Single particle optical response dependence on HAGB density. (a) Electromagnetic simulations of the scattering intensity change with increasing  $\text{Cu}_2\text{O}$  oxide shell thickness,  $\Delta I_{\text{shell}}$ , for a single crystalline Cu nanodisk of five different diameters. The inset is a schematic (not to scale) of the simulated Cu/ $\text{Cu}_2\text{O}$  core-shell model of the nanodisk on a 25-nm silicon nitride layer, mimicking the TEM membrane. (b) Experimentally measured  $\Delta I$  time traces of the 25 particles with 85-nm-diameter during oxidation in 1%  $\text{O}_2$  at  $150^\circ\text{C}$ . The traces are grouped into the response from single crystals (red) and polycrystals (blue). The gray line is a fit to all the single crystalline particle traces based on the JMAK model. (c) Experimental  $\Delta I$  values extracted from the time traces in (b) after 1500 s (25 min) oxidation plotted vs the HAGB density of the 25 analyzed 85-nm particles, revealing a direct correlation. The gray line is a linear fit to the data points.

served as the increasing slope of the single crystal traces in Fig. 5(b), after the initial nucleation of oxide “islands,” indicates a decreasing activation energy for continued oxidation during shell growth, in line with oxide island growth observed on Cu thin films suggesting that nucleation of a new oxide island is more energetically costly than continued oxide growth [44,48,49]. Accordingly, the scaling of  $\Delta I_{\text{shell}}$  with oxidation time  $\tau$  can be described according to the JMAK model as

$$\Delta I_{\text{shell}}(\tau) = C(1 - e^{-(K\tau)^n}), \quad (1)$$

where the conversion factor,  $C = \Delta I_{\text{final}}/\delta_{\text{final}}$ , scales the change of the optical scattering intensity to the volume oxidation fraction,  $\delta$ , obtained from *ex situ* TEM micrographs after oxidation. Hence, fitting Eq. (1) to the  $\Delta I$  traces of the ten single crystalline 85-nm particles reveals that  $n = 1.55$  and  $K = 1.97 \times 10^{-4} \text{ s}^{-1}$  (for equivalent analysis of the 115-nm particles see Figs. S7.3–S7.5 [32]).

As a next step, we expand this analysis to include also the polycrystalline nanoparticles and postulate that the experimentally measured change in integrated scattering intensity  $\Delta I$  can be written as

$$\Delta I(\tau) = [I_{\text{tot}}(\tau) - I_0]/I_0 = \Delta I_{\text{shell}}(\tau) + \Delta I_{\text{HAGB}}(\tau), \quad (2)$$

where  $I_{\text{tot}}(\tau)$  is the total scattering intensity,  $I_0$  is the scattering intensity at the onset of oxidation,  $\Delta I_{\text{shell}}$  is the contribution of the oxide shell growth, which for single crystals is the only contribution (i.e.,  $\Delta I_{\text{shell}} = \Delta I$ ), and  $\Delta I_{\text{HAGB}}$  is the contribution from the presence of HAGBs to the total change in  $\Delta I$ . Hence,  $\Delta I_{\text{HAGB}}$  can be determined from the experiment by subtracting  $\Delta I_{\text{shell}}$  derived from the single crystalline particles from  $\Delta I$  measured for the individual polycrystalline particles. This analysis then reveals that  $\Delta I_{\text{HAGB}}$  decreases linearly (i.e.,

negative  $\Delta I_{\text{HAGB}}$  values) with oxidation time for the polycrystalline 85-nm particles [Fig. 6(a), equivalent  $\Delta I_{\text{HAGB}}$  vs. time of the 115- and 145-nm particles in Fig. S7.6 [32]]. By fitting each  $\Delta I_{\text{HAGB}}$  time trace as

$$\Delta I_{\text{HAGB}}(\tau) = A(L_{\text{HAGB}})\tau, \quad (3)$$

a prefactor  $A$  that depends on the particle specific HAGB grain boundary length,  $L_{\text{HAGB}}$ , can be extracted from the experimental data. Applying this analysis to our three data sets of 85-, 115-, and 145-nm particles then reveals a direct correlation between  $A$  and the HAGB density, for all sizes, which is largely independent from particle size [Fig. 6(b)]. We verify the robustness of the developed model for describing the optical response of single and polycrystalline Cu nanoparticles during the initial oxidation, by modeling two 85-nm polycrystalline particles  $\Delta I$  time traces (the two particles were selected to represent low and high HAGB densities, respectively) using the particle specific HAGB density derived from corresponding TEM images [insets in Figs. 6(c) and 6(d)] and the experimentally obtained parameters, according to

$$\Delta I(\tau) = C(1 - e^{-(K\tau)^n}) + A(L_{\text{HAGB}})\tau. \quad (4)$$

As representative examples, this yields very good agreement for the particle with low HAGB density [Fig. 6(c)] and the particle with high HAGB density [Fig. 6(d)], despite their significantly different  $\Delta I$  temporal evolution. Expanding the treatment to all polycrystals in the 85-, 115-, and 145-nm size particle sets (58 particles in total) yields good agreement for all particles, as manifested in reasonable root-mean-square errors of the predicted  $\Delta I$  time traces (details in Fig. S7.7 [32]). This analysis thus corroborates the conclusion that the optical

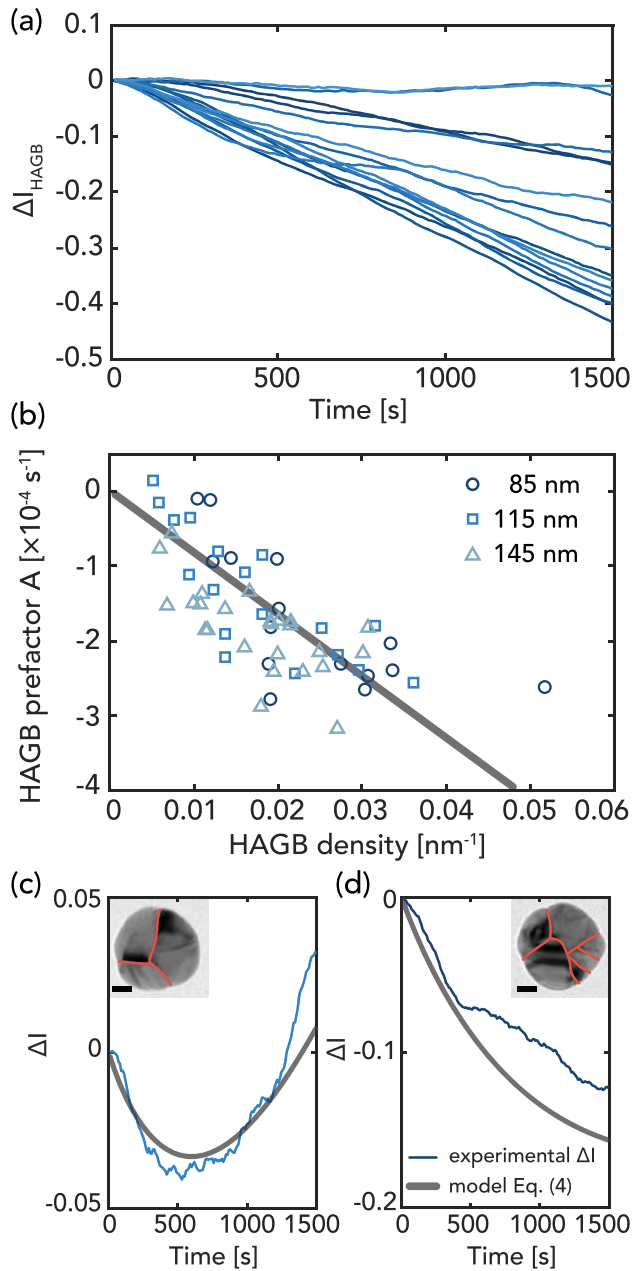


FIG. 6. Extracting the high-angle grain boundary contribution to the overall  $\Delta I$  single particle optical response. (a) Contribution from the presence of HAGBs to the total change in optical response,  $\Delta I_{\text{HAGB}}$ , of the 15 polycrystalline 85-nm particles extracted from their experimentally measured  $\Delta I$  traces using Eq. (2). Note the linear decrease in almost all traces. (b) HAGB prefactor  $A$  extracted by fitting Eq. (3) to the  $\Delta I_{\text{HAGB}}$  time traces for the three data sets of particles with different size (circles: 85-nm, squares: 115-nm, and triangles: 145-nm disks) plotted vs HAGB density. It reveals a direct correlation between these two parameters and quantifies the increasing contribution of HAGBs to the total  $\Delta I$  signal measured during oxidation. The gray line is a linear fit to all data points, yielding  $A = BL_{\text{HAGB}}/A_0$ , where the constant  $B = -0.0081 \text{ nm s}^{-1}$  and  $A_0$  is the initial Cu nanodisk projected area. (c), (d)  $\Delta I$  time traces calculated by our adapted JMAK-optical model [Eq. (4), gray lines] compared to experimentally measured  $\Delta I$  time traces (blue lines) for two polycrystalline particles. Insets: images of the particles before oxidation with scale bars of 20 nm.

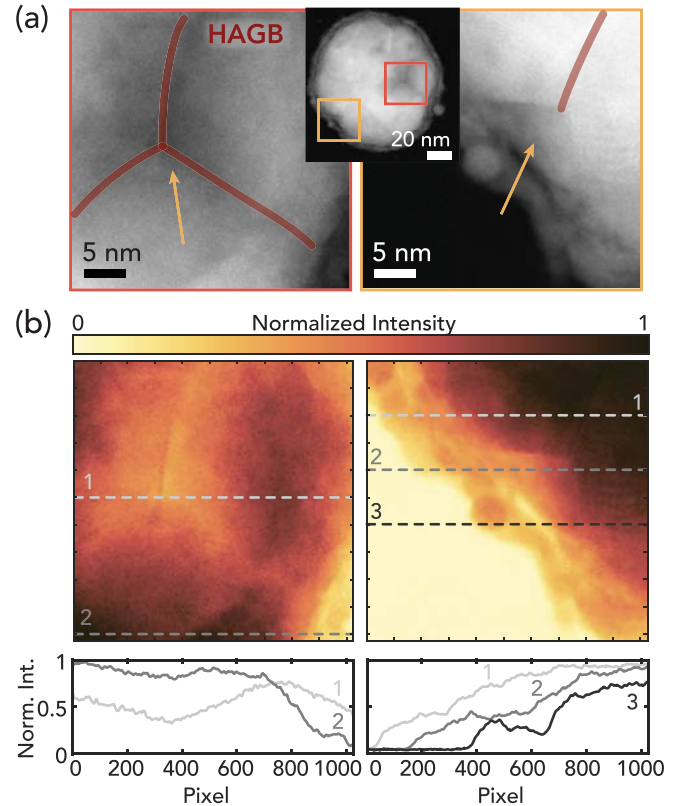


FIG. 7. Concept of grain boundary vacancy accumulation. (a) Two examples of high resolution ADF STEM images revealing a darker contrast at grain boundaries (red lines) in a nanoparticle oxidized for 25 min, as indicated by the arrows. (b) Same STEM images as in (a) but false-colored to increase contrast, such that areas of lower electron scattering cross section are highlighted as bright yellow. Extracting the electron scattering cross section along the two lines indicated in the left images reveals more than 50% lower intensity in the center (line 1), compared to the left corner (line 2) of the image. In the right micrograph, a wedge-formed area of lower electron scattering is revealed at the grain boundary–oxide shell intersection, which suggests either inward oxide growth along the grain boundary or vacancy accumulation (further examples in Fig. S9.2 [32]).

$\Delta I$  response of polycrystalline particles is the combination of a contribution from oxide shell growth, which leads to an increase of  $\Delta I$ , and a second process, which is absent in the single crystals and leads to a decrease of  $\Delta I$ .

To finally unravel the origin of the impact of HAGBs on the  $\Delta I$  time traces of the individual particles discussed above, and thereby understand the mechanistic role of the HAGBs during oxidation of polycrystalline nanoparticles, we start out by noting that thermal annealing of the particles, as we routinely execute prior to our oxidation experiments, significantly reduces defect density and grain boundary length through recrystallization, which results in a narrow plasmon resonance (examples in Fig. S8.1 [32]) [50]. Subsequently, as we expose the annealed particles to  $\text{O}_2$  to induce the oxidation process, the defect density at the HAGBs is again increasing due to either vacancy accumulation or oxide growth, as revealed by annular dark-field scanning transmission electron microscopy (ADF STEM) imaging [Fig. 7(a) and further examples in

Fig. S9.2 [32]]. Specifically, analysis of STEM micrographs of particles after oxidation reveals areas of more than 50% lower electron scattering cross sections at the HAGBs [Fig. 7(b)], which are not observed before oxidation (Fig. S9.1 [32]). This effect can in principle be explained by two different factors: (i) local depletion of Cu atoms, i.e., vacancy accumulation in the HAGB region, or (ii) formation of oxide in the HAGB region, resolved due to the atomic number contrast and possible strain induced by volume expansion [51,52]. *A priori* it is difficult to completely rule out one of these mechanisms. However, by again resorting to our DFT calculations, we can conclude that Cu vacancies are preferably formed at undercoordinated sites, due to the difference in the Cu vacancy formation energy for Cu(100) and Cu(911) (0.43 and 0.29 eV, respectively) compared to the vacancy formation energy in Cu bulk (1.08 eV). This difference in vacancy formation energies thus supports a mechanism of preferential accumulation of vacancies at the grain boundary sites. In view of the DFT energetics, as well as the fact that we indeed observe a homogeneous oxide shell growth to a thickness that is independent of the grain structure of the individual particles, it is therefore unlikely that a significant amount of oxide forms at the HAGBs. Moreover, in cases where the grain boundary is not associated with undercoordinated metal atoms, vacancies provide a mechanism to release the strain that builds up at grain boundaries [53], from which we also can exclude that the observed contrast in the STEM images is due to lattice strain.

Accepting vacancy accumulation in the HAGB region during oxidation as the dominant mechanism, we can now explain the observed decrease of the optical scattering intensity  $\Delta I$  of polycrystalline nanoparticles as a consequence of vacancy accumulation in the HAGB regions and a corresponding increase in absorption losses (and thus reduced scattering). The increased absorption loss due to vacancy accumulation is in qualitative agreement with earlier reports about the attenuation of the plasmon resonance by the presence of vacancy sites [50,54–57]. Specifically, we propose vacancy accumulation along the grain boundaries and the formation of conelike vacancy clusters at HAGB junctions at the grain boundary–oxide shell interface during the early stage of oxidation considered here (Fig. 7). Subsequently, at later oxidation stages when high enough vacancy density is reached, one or several of these vacancy clusters will continue to grow into a nanoscale Kirkendall void. In contrast, for single crystalline particles where HAGBs acting as vacancy sinks are absent, we propose that the Cu vacancies instead accumulate along the metal–oxide shell interface. To this end, DFT calculations reveal that the vacancies are less thermodynamically stable on well-coordinated sites, and we can thus speculate that the vacancies diffuse across the oxide shell to the oxide surface.

To further corroborate the hypothesis that the formation of vacancy clusters at HAGBs can explain the evolution of the optical scattering cross section of polycrystalline Cu nanoparticles observed in our experiments, we combine classical electromagnetic and *ab initio* calculations to obtain the optical response of Cu nanodisks with different configurations of HAGB vacancy clusters. First, we estimate the difference between the complex permittivity of pure Cu,  $\epsilon_{\text{Cu}}$ , and that of Cu with 12.5% vacancy accumulation,  $\epsilon_{\text{Cu}}^{12.5\%}$ , using *ab*

*initio* calculations (see Sec. S10 of the Supplemental Material for details and Ref. [58–64]). We specifically choose 12.5% as the proportion of vacancies because it allows us to use a relatively small unit cell with seven atoms and one vacancy for the permittivity calculation. The *ab initio* calculations reveal that the presence of vacancies leads to a significantly larger imaginary part of  $\epsilon_{\text{Cu}}^{12.5\%}$ , thereby indeed giving rise to larger absorption losses (calculated dielectric functions in Fig. S10.1 [32]). We then model the plasmonic response of a polycrystalline Cu disk by using the calculated  $\epsilon_{\text{Cu}}^{12.5\%}$  to describe regions of vacancy accumulation at HAGB clusters with different geometries (schematics in Fig. 8), and  $\epsilon_{\text{Cu}}$  elsewhere in the disk, and obtain the resulting optical cross section by solving Maxwell’s equations using COMSOL Multiphysics [42].

As a specific example of such a calculation, we present a comparison of the optical scattering cross section spectrum of a pristine Cu disk with diameter  $D_0 = 85$  nm and height  $h = 40$  nm [black dashed line in Fig. 8(a)], and that of an identical disk with two orthogonal  $t = 5$ -nm-wide HAGB volumes with the 12.5% level of vacancy accumulation (drawn as a blue cross in the schematics) modeled by the corresponding permittivity we have calculated (dark blue spectrum). As the main result, we observe a clear decrease of the optical cross section upon vacancy accumulation at the HAGBs, with a change of the integrated intensity  $\Delta I_{\text{HAGB}} \approx -20\%$ , in good qualitative agreement with our experimental results.

To now compare this value with the positive  $\Delta I_{\text{Shell}}$  change induced by oxide shell growth, first, we calculated the thickness of the  $\text{Cu}_2\text{O}$  shell that is necessary to create the number of Cu vacancies present in the two HAGBs. For the simulated 12.5% level of vacancy accumulation, we find the oxide thickness to be 0.42 nm (see Sec. S11 [32] and Ref. [65] for details). Comparing this number with the calculated  $\Delta I_{\text{Shell}}$  increase as function of oxide layer thickness [cf. Fig. 5(a)] reveals that a 0.42-nm-thick oxide layer would induce  $\Delta I_{\text{Shell}} \approx +5\%$ . Since this number is much smaller than the  $\Delta I_{\text{HAGB}} \approx -20\%$  induced by the HAGB vacancy accumulation, we conclude that the additional absorption losses induced by the vacancies are able to overcompensate the increase due to the oxide layer  $\Delta I_{\text{Shell}}$ , thus resulting in a net decrease of the integrated intensity similar to the experimental measurements of the polycrystalline disks (cf. Figs. 5–6). To further verify that the HAGB vacancy induced decrease  $\Delta I_{\text{HAGB}}$  indeed can overcompensate the  $\Delta I_{\text{Shell}}$  observed for single crystals (cf. Fig. 5), we also explicitly calculated the optical scattering cross section for a Cu disk with two orthogonal  $t = 5$ -nm-wide grain boundary regions and encapsulated by a 1-nm-thick  $\text{Cu}_2\text{O}$  oxide layer (Fig. 8(a), bright blue line). The oxide thickness corresponds to assuming that 42% of the Cu atoms in the oxide originate from a vacancy that accumulate at the HAGB. We find also for this scenario a net decrease of  $\Delta I \approx -11\%$ . Finally, we note that the current model focuses on capturing the increase in absorption losses due to vacancy accumulation, but that the vacancies may further decrease  $\Delta I$  via, for example, absorption losses due to surface roughness [57], which we have not explicitly treated here.

As the last step, we investigate to what extent grain boundary and vacancy cluster configurations with different geometries and localization in different regions of the Cu disk

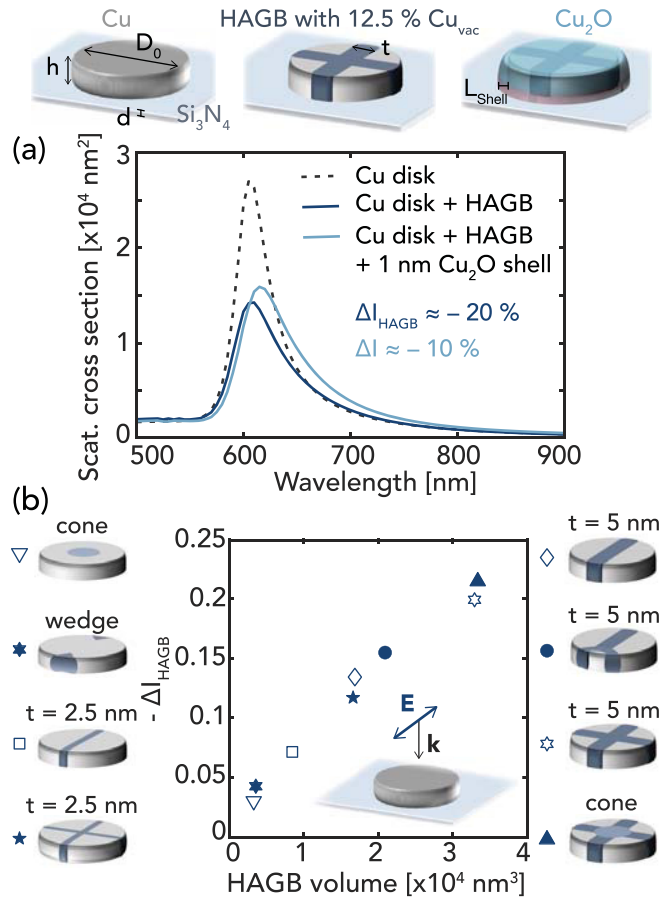


FIG. 8. Electromagnetic calculations of vacancy accumulation at HAGBs. (a) Calculated optical scattering cross section of a pristine metallic Cu nanodisk with diameter  $D_0 = 85$  nm and height 40 nm (dashed line), and of a Cu nanodisk with the same size with 12.5% vacancy accumulation along two HAGBs without (dark blue) and with (bright blue) an encapsulating  $\text{Cu}_2\text{O}$  oxide shell. The decrease of the scattering cross section is 20% for the disk with vacancy accumulation at the HAGBs and only 10% when adding the oxide layer. The simulated models are schematically illustrated on top of the graph, showing the HAGBs with a  $t = 5$ -nm wide volume of 12.5% vacancy density (drawn in dark blue), forming an orthogonal cross in the plane parallel to the substrate. The added oxide shell is pictured as a transparent layer in the right schematic, with a thickness of  $L_{\text{Shell}} = 1$  nm. (b) Calculated  $\Delta I_{\text{HAGB}}$  for different HAGB and vacancy cluster configurations as shown by the schematics, all modeled for a homogeneous 12.5% level vacancy accumulation. These calculations were performed without oxide shell for simplicity. A more detailed discussion of the different geometries can be found in Sec. S11. The obtained  $\Delta I_{\text{HAGB}}$  values are plotted for each configuration as functions of the volume of the vacancy clusters,  $V_{\text{HAGB}}$ . In (a) and (b) all disks are placed on a  $d = 25$ -nm-thick silicon nitride substrate to emulate the experimental scenario and the illumination is linearly polarized. The direction of polarization is indicated in the inset in (b) and affects the results only weakly (see Sec. S12 for details).

influence the amount of  $\Delta I$  reduction [Fig. 8(b); note that we did not include an oxide shell here to focus on the effect of the vacancies alone, and that all other parameters are the same as for the calculations in Fig. 8(a); for further details see Sec. S11 [32]]. We then plot the calculated  $\Delta I_{\text{HAGB}}$  for

each HAGB vacancy accumulation configuration as functions of its total volume  $V_{\text{HAGB}}$ , which ranges between 2% and 13% of the total particle volume [Fig. 8(b)]. As the main result, we see that  $\Delta I_{\text{HAGB}}$  scales approximately linearly with  $V_{\text{HAGB}}$ , with significant values of  $|\Delta I_{\text{HAGB}}|$  also for relatively small  $V_{\text{HAGB}}$ . Interestingly, the results are also quite insensitive to the incident polarization (equivalent calculations for the orthogonal incident polarization in Fig. S12.1 [32]) or the particular HAGB geometry. Furthermore, we note that doubling the vacancy density at the HAGBs results in an approximately doubled decrease of  $\Delta I_{\text{HAGB}}$  (see Sec. S13 for details [32]). The theoretical calculations thus clearly suggest that the main parameter governing the change of  $\Delta I_{\text{HAGB}}$  during the oxidation process is the total number of vacancies in the vacancy clusters associated with the HAGBs, which is in very good qualitative agreement with the experimental results, where we indeed have identified a linear relation between  $\Delta I_{\text{HAGB}}$  and HAGB density [cf. Fig. 5(c)], and that finer details of HAGB geometry or localization within the particle are less important.

### III. SUMMARY AND CONCLUSIONS

In summary, we have investigated the role of HAGBs in the oxidation of nanofabricated polycrystalline Cu nanoparticles in the 100-nm size range at  $150^\circ\text{C}$  in 1%  $\text{O}_2$  in Ar carrier gas, using a combination of *in situ* single particle plasmonic nanoimaging and *postmortem* TEM image analysis, as well as *ab initio* and electromagnetic calculations. As the first main experimental result, we found that during the initial stage of oxidation a homogeneous oxide shell layer is growing at a grain morphology independent rate to a thickness of about 5 nm. This is in good agreement with the Cabrera-Mott oxidation mechanism and in line with previous reports for nanocrystalline Cu thin films [13,36]. Based on DFT calculations, we explain this grain morphology independence of the oxide shell growth rate by the extraction of Cu atoms from the metal lattice being the rate limiting step, rather than the diffusion of ions. That Cu atom extraction is the rate limiting step has the key consequence that the marginally higher diffusion rate of Cu atoms along HAGBs compared to their diffusion in the Cu lattice does not decrease the overall oxidation activation energy and thus has no impact on the oxide shell growth rate.

As the second main result, we found distinctly different optical response measured *in situ* during oxidation of individual single crystalline Cu particles compared to polycrystalline ones. Specifically, the measured change in integrated optical scattering intensity,  $\Delta I$ , can be deconvoluted into a contribution imposed by the growth of the oxide layer, which leads to an increase of  $\Delta I$ , and a contribution from HAGBs, which leads to a decrease of  $\Delta I$ . The optical scattering decrease is proportional to the HAGB density in the individual polycrystalline nanoparticles and completely absent in the single crystalline ones. Mechanistically, we identified the accumulation of Cu vacancies along HAGBs and at HAGB-oxide shell intersections as the reason for this optical effect, induced by the consequent plasmon damping by increased absorption losses and concurrent decrease in scattering intensity  $\Delta I$ . This hypothesis was corroborated by electromagnetic calculations based on a local modification of the Cu permittivity associated

with the formation of vacancy clusters along the HAGBs. Indeed, the vacancy clusters can explain the increased absorption losses and yield a negative  $\Delta I$  that is proportional to the simulated vacancy accumulation volume at HAGBs. Hence, as the third main result, we conclude that the experimentally measured change of  $\Delta I$  likely directly reports the accumulation of vacancies along HAGBs and at HAGB–oxide shell intersections during oxidation.

Finally, we predict that the identified conelike areas of high vacancy density at the HAGB–oxide intersection areas serve as nuclei for the formation of Kirkendall voids in polycrystalline Cu nanoparticles at later stages of oxidation not explicitly studied here. In contrast, for single crystalline particles absent of HAGBs acting as vacancy sinks, we propose that the Cu vacancies instead accumulate along the metal core–oxide shell interface. Based on our DFT calculations, we predict that the vacancies are less thermodynamically stable on well-coordinated sites and we speculate that the vacancies diffuse across the oxide shell to a higher degree.

In a wider perspective, our results highlight the potential of localized surface plasmon-based single particle *in situ* spectroscopy and imaging techniques as a tool to investigate the role of grain boundaries in nanomaterials due to the demonstrated exceptional sensitivity towards grain boundary processes. Such processes are likely of high importance in metal-hydrogen interactions [66], nanoelectronics [20], nanosensors [18], nanostructured battery electrodes [21], and in nanostructure model systems in heterogeneous catalysis [22].

## IV. METHODS

### A. *In situ* dark-field plasmonic nanoimaging

The *in situ* plasmonic microscopy oxidation reaction was conducted in a Linkam reaction cell (THMS600) with optical access, mounted on an upright Nikon Eclipse LV150 N microscope and connected to mass flow controllers (Bronkhorst, low- $\Delta P$ -flow) to regulate the supplied gas mixture at atmospheric pressure. To achieve the 1% O<sub>2</sub>, 15% ( $\pm 2$  relative %) O<sub>2</sub> was diluted by Ar (6.0 purity) and similarly 100% H<sub>2</sub> was diluted to 2% in Ar during the thermal annealing. To enable plasmonic microscopy, the microscope was equipped with a dark-field objective (Nikon TU plan ELWD 50 $\times$ , NA = 0.60, WD = 11 mm) and light was collected by an Andor Newton 920 charge-coupled device (CCD) camera (256  $\times$  1024 pixels). The scattering image,  $F_{\text{raw}}$ , from the particles illuminated by a 50-W halogen light source to achieve white light, was collected as an image of the sample every 10 s (0.25 s exposure with 30 accumulations). The CCD dark current,  $F_{\text{dark}}$ , was collected as an image without illuminating the CCD and subtracted from the raw image frames to yield the scattering intensity frames as  $F_{\text{scat}} = F_{\text{raw}} - F_{\text{dark}}$ . A particle finding algorithm based on a wavelet filter was used in the first frame. In each frame,  $F_{\text{scat}}$ , the normalized scattering intensity per pixel at each particle, was collected from a box of 7  $\times$  7 pixels and normalized as  $\tilde{I}_p = I_p/49$ , and the background scattering was collected in a frame with sides 9  $\times$  9 pixels outside the particle box (i.e., not including the particle box = 32 pixels),  $\tilde{I}_b = I_b/32$ , thus  $\tilde{I}_{\text{Cu}} = \tilde{I}_p - \tilde{I}_b$ . On the sample chip, there was an additional array of 25 Au nanodisks which served to normalize for illumination fluctuations. The scattering intensities

of the Au particles,  $\tilde{I}_{\text{Au}}$ , were collected equivalently to the Cu particles with a corresponding background intensity. Finally, the scattering intensity from Cu nanoparticle  $j$  during the oxidation was calculated as  $\tilde{I}_j = \tilde{I}_{\text{Cu}, j} / \text{mean}(\tilde{I}_{\text{Au}})$ .

### B. Sample nanofabrication

TEM compatible substrates comprised of a 25-nm-thin SiN<sub>x</sub> film grown on a Si wafer, in which a 120  $\times$  120  $\mu\text{m}$  square was etched, were fabricated in-house following the recipe developed by Grant *et al.* [31]. By means of electron beam lithography, arrays of 5  $\times$  5 nanoparticles were fabricated onto these silicon nitride thin film membranes according to the following fabrication procedure: (1) A thin film of copolymer MMA (8.5) MMA (MicroChem Corporation, 10 wt % diluted in anisole) was spin coated at 6000 rpm for 60 s and followed by baking on a hotplate at 180°C for 5 min. This was followed by spin coating polymethyl methacrylate (PMMA) A2 at 3000 rpm for 60 s and baking at 180°C for 5 min. (2) The resist was patterned by electron-beam exposure in a JEOL JBX 9300FS (2 nA with a shot pitch of 2 nm, 2000 mC/cm<sup>2</sup> exposure dose). (3) The pattern was developed in methyl isobutyl ketone (MIBK) : isopropanol (1:3) for 120 s, followed by drying under N<sub>2</sub> stream. (4) Either a 20-nm Au thin film or a 40-nm Cu thin film, depending on whether fabricating the Au reference particles or the Cu nanoparticles, was deposited by electron beam evaporation in a Lesker PVD 225 at a rate of 1–2 Å/s and liftoff was done in acetone for approximately 12 h. (5) Finally, to achieve the grain morphologies, the sample was annealed in 2% H<sub>2</sub> mixed in Ar at 400°C for 2 h.

### C. Electromagnetic calculations

We performed three-dimensional electromagnetic simulations based on the finite element method (FEM), as implemented in the commercial COMSOL Multiphysics software [42]. We solved Maxwell's equations in the frequency domain, using the radio frequency module (RF Module). The optical constants for pure Cu, Cu<sub>2</sub>O, and Si<sub>3</sub>N<sub>4</sub> used in the calculations were obtained from experimental data available from Refs. [67–69].

To study the shift of the scattering resonance due to the oxide shell thickness [Fig. 5(a)], we used a model geometry consisting of a rounded Cu disk of diameter 80, 100, 120, 140, and 160 nm, and height 40 nm with an edge curvature of 5 nm. The Cu nanodisk was placed on a 25-nm-thin silicon nitride film.

To study the effect of vacancy accumulation in the HAGBs (Fig. 8), the change to the permittivity of copper caused by the 12.5% vacancy accumulation was obtained from *ab initio* calculations (Sec. S10 of the Supplemental Material). The exact simulation geometry for each configuration is described in Sec. S11. The full simulation region considered in all calculations was a sphere of radius 2000 nm, surrounded by a 600-nm-thick perfectly matched layer (PML). The optical scattering cross section was calculated from integration over a large closed spherical surface of the scattered Poynting vector associated with the nanodisk upon illumination.

#### D. Transmission electron microscopy acquisition

Imaging of Cu nanoparticles in the annealed and oxidized state was conducted in a FEI Tecnai T20 with LaB<sub>6</sub> filament and operated at 200 kV. The sample was taken directly from the reaction cell after thermal annealing (400 °C in 2% H<sub>2</sub> /98% Ar) to the microscope in order to minimize hydrocarbon polymer deposition and cross-linking by the electron beam. The imaging was done in bright-field mode at a magnification of 43 kx using an objective aperture to reduce diffraction ghost images. The high resolution bright-field imaging, selected area electron diffraction, and annular dark-field scanning transmission electron microscopy (ADF STEM) was acquired in a probe corrected FEI Titan 80–300, with a field emission gun (FEG) electron source operated at 300 kV. The ADF STEM imaging was at a camera length of 195 mm.

#### E. TEM image analysis

From bright-field TEM micrographs of thermally annealed Cu nanoparticles, the high-angle grain boundary length was measured in MATLAB (versions 2019b and 2020b) using the image processing toolbox (function *drawassisted*). Oxide shell thickness,  $L_{\text{shell}}$ , was measured by drawing the inner and outer limits of the oxide shell using ImageJ in each TEM image and calculating the effective thickness from this area,  $A_{\text{shell}}$ , as  $L_{\text{shell}} = A_{\text{shell}}/(\pi D_0)$  for each particle initial diameter  $D_0$ , assuming a smooth oxide edge. The particle area before oxidation was measured using the image processing toolbox in MATLAB; images were morphologically filtered (function *imopen*, structure element: disk, radius 5 pixels) to reduce noise close to the particle edge and the boundary was detected (using *bwboundaries*). A circle was fitted to the detected perimeter to calculate the initial particle diameter  $D_0$ .

#### F. Transmission Kikuchi diffraction analysis

Prior to the scanning electron microscope (SEM) investigation the 25-nm silicon nitride TEM windows with the Cu nanoparticles were coated on the back side (opposite side to the particles) with 3 nm of chromium to reduce charging during the TKD experiments. All TEM membranes were mounted on a multigrid holder able to hold six samples simultaneously for the TKD investigations. The samples were mounted so that the Cu nanoparticles were facing downward (opposite to the incoming electron beam), as such configuration is known to enhance the diffraction signal from the Cu particles [70]. The holder was installed on a FEI Nova Nano lab 600 stage, in a way that the samples were positioned horizontally (0° tilt). During the experiment, a cryocan was constantly filled with liquid nitrogen to prevent contamination of the particles.

The TKD experiment was conducted at an acceleration voltage of 30 kV with a 30- $\mu\text{m}$  aperture resulting in a probe current of 3.3 nA. The OPTIMUS TKD detector from Bruker Nano GmbH was positioned in such a way that the smallest distance between the electron-beam focusing point at the specimen surface and the camera was 14 mm at a working distance of 5 mm. Each particle was measured for approximately 30 s with a pattern resolution of 400 × 300

pixels (4 × 4 binning), exposure time of 10 ms, and step size of 5 nm.

Previous to the data analysis, the raw data were processed to remove uncertain data points and to define grains. First, all data sets containing less than three points were removed from the raw orientation map; subsequently the data were cleaned by dilating the data points that did not belong to any grain but had neighbors belonging to an indexed grain. Such cleanup was performed in a single interaction only changing the orientation of single nonindexed points which were surrounded by valid grains. A grain was defined as an area containing at least three data points with a misorientation larger than 15° with respect to its neighbor. The data processing was performed using CRYSTALIGN BRUKER and OIM TSL software.

#### G. Density functional theory calculations

DFT calculations were performed using the Vienna *ab initio* simulation package (VASP) [71–74]. The Kohn-Sham orbitals were expanded in a plane wave basis and truncated at a kinetic energy of 480 eV. Interaction between the core and valence electrons was described with the use of projector augmented wave potentials (PAWs) [75,76]. O and Cu were treated with 6 and 11 electrons in the valence, respectively. The Brillouin zone integration was approximated by finite sampling, using the Monkhorst-Pack scheme [77].

The exchange correlation energy was calculated within the Perdew, Burke, and Ernzerhof (PBE) formulation [78]. Given the localized nature of the electronic states on Cu<sub>2</sub>O, a Hubbard correction was applied to the Cu 3d states to correct for the self-interaction error in the semilocal functional. A Hubbard correction of  $U_{\text{eff}} = 6$  eV was used [79], which was shown to capture experimental values for the lattice constant and peak position of the density of states. The Hubbard-corrected functional was used to investigate the nature and diffusion of Cu vacancies on Cu<sub>2</sub>O. A  $k$ -point grid of 3 × 3 × 3 (5 × 5 × 5) was used for bulk Cu (Cu<sub>2</sub>O), whereas a grid of 4 × 4 × 1 and 4 × 8 × 1 was used for Cu(100) and Cu(911), respectively. Methfessel and Paxton (Gaussian) smearing of 0.1 (0.05) eV was applied to the metallic (oxide) systems, respectively. The system total energy was considered converged when the energy difference between steps was smaller than 10<sup>-6</sup> eV. Structural optimization was performed with the use of the conjugate gradient method and structural optimization was reached when the forces on the atoms were smaller than 0.01 eV/Å. Activation energies were calculated with the use of the climbing-image nudge elastic band (CI-NEB) technique [80]. Seven images were used along the reaction coordinate to calculate the minimum energy path. A force convergence criterion of 0.05 eV/Å was used for the calculation of the activation energies and the nature of the transition state was confirmed by vibrational analysis.

A 4 × 4 × 4 (2 × 2 × 2) unit cell was used to investigate bulk Cu (Cu<sub>2</sub>O). Cu(100) and Cu(911) were modeled with a (4 × 4) and (2 × 1) surface cell and described with seven layers each. The bottom two layers were constrained to bulk positions for all surface calculations. The slabs were separated by at least 15 Å of vacuum. The equilibrium lattice constant of Cu (Cu<sub>2</sub>O) was determined to be 3.64 (4.27) Å, in good agreement with previous reports at the same level of theory [39,79].

The energy of formation for a neutral vacancy was calculated as [81]

$$\Delta E_F = E_{\text{def}} - E_{\text{prist}} - \sum_i \Delta n_i \mu_i,$$

where  $E_{\text{def}}$  is the energy of the defective system with a vacancy,  $E_{\text{prist}}$  is the energy of the pristine system, and  $\Delta n_i \mu_i$  refers to the change in number of the Cu atoms (removed or added) between the defective and the pristine systems, with an associated chemical potential  $\mu_i$ . The chemical potential  $\mu_i$  accounts for the energetic cost of transferring an atom of the  $i$ th species to or from a thermodynamic reservoir. In this study we have assumed that all Cu atoms are transferred to Cu metallic bulk. We have, thus, fixed the chemical potential for Cu atoms as the energy of the bulk per Cu atom. In Fig. 4(b), the final state (Cu at  $\text{Cu}_2\text{O}$ ) was calculated as the energy of formation of Cu in the respective metallic surface minus the

energy of formation of a single Cu vacancy in  $\text{Cu}_2\text{O}$ , both at the PBE level.

## ACKNOWLEDGMENTS

This research has received funding from the Knut and Alice Wallenberg Foundation, Project No. 2015.0055. M.Z.H., J.A., and R.E.L. acknowledge financial support by Grant No. PID2019-107432GB-I00 funded by MCIN/AEI/10.13039/501100011033/. V.M.S. acknowledges financial support by Grant No. PID2019105488GBI00 funded by MCIN/AEI/10.13039/501100011033/. Part of this work was carried out at the MC2 cleanroom facility and at the Chalmers Materials Analysis Laboratory.

The manuscript was written through contributions of all authors. All authors have given approval to the final version of the manuscript.

- 
- [1] Y. Zeng, K. Bai, and H. Jin, Thermodynamic study on the corrosion mechanism of copper wire bonding, *Microelectron. Reliab.* **53**, 985 (2013).
- [2] B. D. Anderson and J. B. Tracy, Nanoparticle conversion chemistry: Kirkendall effect, galvanic exchange, and anion exchange, *Nanoscale* **6**, 12195 (2014).
- [3] M. Muzzio, J. Li, Z. Yin, I. M. Delahunty, J. Xie, and S. Sun, Monodisperse nanoparticles for catalysis and nanomedicine, *Nanoscale* **11**, 18946 (2019).
- [4] S. Alekseeva, I. I. Nedrygailov, and C. Langhammer, Single particle plasmonics for materials science and single particle catalysis, *ACS Photonics* **6**, 1319 (2019).
- [5] J. Dou, Z. Sun, A. A. Opalade, N. Wang, and W. Fu, and F. (Feng) Tao, Operando chemistry of catalyst surfaces during catalysis, *Chem. Soc. Rev.* **46**, 2001 (2017).
- [6] G. G. Jernigan and G. A. Somorjai, Carbon monoxide oxidation over three different oxidation states of copper: metallic copper, copper (I) oxide, and copper (II) oxide - a surface science and kinetic study, *J. Catal.* **147**, 567 (1994).
- [7] A. P. Lagrow, D. C. Lloyd, D. Schebarchov, P. L. Gai, and E. D. Boyes, *In situ* visualization of site-dependent reaction kinetics in shape-controlled nanoparticles: Corners vs edges, *J. Phys. Chem. C* **123**, 14746 (2019).
- [8] Y. Yin, R. M. Rioux, C. K. Erdonmez, S. Hughes, G. A. Somorjai, and A. P. Alivisatos, Formation of hollow nanocrystals through the nanoscale Kirkendall effect, *Science* **304**, 711 (2004).
- [9] R. Nakamura, D. Tokozakura, H. Nakajima, J.-G. Lee, and H. Mori, Hollow oxide formation by oxidation of Al and Cu nanoparticles, *J. Appl. Phys.* **101**, 074303 (2007).
- [10] J. G. Railsback, A. C. Johnston-Peck, J. Wang, and J. B. Tracy, Size-dependent nanoscale Kirkendall effect during the oxidation of nickel nanoparticles, *ACS Nano* **4**, 1913 (2010).
- [11] J. Horváth, R. Birringer, and H. Gleiter, Diffusion in nanocrystalline material, *Solid State Commun.* **62**, 319 (1987).
- [12] Y. Niu, F. Gesmundo, G. Farnè, Y. S. Li, P. Matteazzi, and G. Randi, The air oxidation of a nanocrystalline Cu-10 Wt%Ni alloy at 800°C, *Corros. Sci.* **42**, 1763 (2000).
- [13] Z. Han, L. Lu, H. W. Zhang, Z. Q. Yang, F. H. Wang, and K. Lu, Comparison of the oxidation behavior of nanocrystalline and coarse-grain copper, *Oxid. Met.* **63**, 261 (2005).
- [14] L. Novotny and N. van Hulst, Antennas for light, *Nat. Photonics* **5**, 83 (2011).
- [15] C. Wadell, S. Syrenova, and C. Langhammer, Plasmonic hydrogen sensing with nanostructured metal hydrides, *ACS Nano* **8**, 11925 (2014).
- [16] A. Tittl, H. Giessen, and N. Liu, Plasmonic gas and chemical sensing, *Nanophotonics* **3**, 157 (2014).
- [17] K. M. Mayer and J. H. Hafner, Localized surface plasmon resonance sensors, *Chem. Rev.* **111**, 3828 (2011).
- [18] T. Hübert, L. Boon-Brett, G. Black, and U. Banach, Hydrogen sensors - A review, *Sens. Actuators, B* **157**, 329 (2011).
- [19] M. Benelmekki and A. Erbe, Nanostructured thin films—background, preparation and relation to the technological revolution of the 21st century, in *Frontiers of Nanoscience*, (Elsevier, Amsterdam, Netherlands, 2019), Vol. 14, pp. 1–34.
- [20] Y. Chen, Nanofabrication by electron beam lithography and its applications: A review, *Microelectron. Eng.* **135**, 57 (2015).
- [21] C. Zhu, R. E. Usiskin, Y. Yu, and J. Maier, The nanoscale circuitry of battery electrodes, *Science* **358**, aao2808 (2017).
- [22] S. Alayoglu, J. M. Krier, W. D. Michalak, Z. Zhu, E. Gross, and G. A. Somorjai, *In situ* surface and reaction probe studies with model nanoparticle catalysts, *ACS Catal.* **2**, 2250 (2012).
- [23] W. Karim, S. Tschupp, J. Herranz, T. Schmidt, Y. Ekinici, and J. van Bokhoven, State-of-the-art nanofabrication in catalysis, *Chim. Int. J. Chem.* **71**, 160 (2017).
- [24] C.-L. Huang, W.-L. Weng, C.-N. Liao, and K. N. Tu, Suppression of interdiffusion-induced voiding in oxidation of copper nanowires with twin-modified surface, *Nat. Commun.* **9**, 340 (2018).
- [25] V. P. Zhdanov and B. Kasemo, Cabrera–Mott kinetics of oxidation of nm-sized metal particles, *Chem. Phys. Lett.* **452**, 285 (2008).
- [26] A. P. LaGrow, M. R. Ward, D. C. Lloyd, P. L. Gai, and E. D. Boyes, Visualizing the Cu/Cu<sub>2</sub>O interface transition in nanoparticles with environmental scanning transmission electron microscopy, *J. Am. Chem. Soc.* **139**, 179 (2017).

- [27] S. Sharna, M. Bahri, C. Bouillet, V. Rouchon, A. Lambert, A. S. Gay, D. Chiche, and O. Ersen, *In situ* STEM study on the morphological evolution of copper-based nanoparticles during high-temperature redox reactions, *Nanoscale* **13**, 9747 (2021).
- [28] A.-A. El Mel, L. Molina-Luna, M. Buffière, P.-Y. Tessier, K. Du, C.-H. Choi, H.-J. Kleebe, S. Konstantinidis, C. Bittencourt, and R. Snijders, Electron beam nanosculpting of Kirkendall oxide nanochannels, *ACS Nano* **8**, 1854 (2014).
- [29] R. F. Egerton, P. Li, and M. Malac, Radiation damage in the TEM and SEM, *Micron* **35**, 399 (2004).
- [30] J. Cure, A. Glaria, V. Collière, P. F. Fazzini, A. Mlayah, B. Chaudret, and P. Fau, Remarkable decrease in the oxidation rate of Cu nanocrystals controlled by alkylamine ligands, *J. Phys. Chem. C* **121**, 5253 (2017).
- [31] A. W. Grant, Q.-H. Hu, and B. Kasemo, Transmission electron microscopy windows for nanofabricated structures, *Nanotechnology* **15**, 1175 (2004).
- [32] See Supplemental Material at <http://link.aps.org/supplemental/10.1103/PhysRevMaterials.6.045201> for more details and additional figures of the optical scattering data analysis, density functional theory, and the electromagnetic calculations.
- [33] J. Li and C. Liu, Carbon-coated copper nanoparticles: synthesis, characterization and optical properties, *New J. Chem.* **33**, 1474 (2009).
- [34] S. Nilsson, D. Albinsson, T. J. Antosiewicz, J. Fritzsche, and C. Langhammer, Resolving single Cu nanoparticle oxidation and Kirkendall void formation with *in situ* plasmonic nanospectroscopy and electrodynamic simulations, *Nanoscale* **11**, 20725 (2019).
- [35] D. Albinsson, A. Boje, S. Nilsson, C. Tiburski, A. Hellman, H. Ström, and C. Langhammer, Copper catalysis at operando conditions—bridging the gap between single nanoparticle probing and catalyst-bed-averaging, *Nat. Commun.* **11**, 4832 (2020).
- [36] B. Maack and N. Nilius, Impact of granularity on the oxidation kinetics of copper, *Phys. Status Solidi* **257**, 1900778 (2020).
- [37] N. Cabrera and N. F. Mott, Theory of the oxidation of metals, *Rep. Prog. Phys.* **12**, 163 (1949).
- [38] X. Duan, O. Warschkow, A. Soon, B. Delley, and C. Stampfl, Density functional study of oxygen on Cu(100) and Cu(110) surfaces, *Phys. Rev. B* **81**, 075430 (2010).
- [39] A. Posada-Borbón, B. Hagman, A. Schaefer, C. Zhang, M. Shipilin, A. Hellman, J. Gustafson, and H. Grönbeck, Initial oxidation of Cu(100) studied by x-ray photo-electron spectroscopy and density functional theory calculations, *Surf. Sci.* **675**, 64 (2018).
- [40] A. Soon, X. Y. Cui, B. Delley, S. H. Wei, and C. Stampfl, Native defect-induced multifarious magnetism in nonstoichiometric cuprous oxide: First-principles study of bulk and surface properties of  $\text{Cu}_{2-\delta}\text{O}$ , *Phys. Rev. B* **79**, 035205 (2009).
- [41] A. F. Wright and J. S. Nelson, Theory of the copper vacancy in cuprous oxide, *J. Appl. Phys.* **92**, 5849 (2002).
- [42] COMSOL, COMSOL Multiphysics v. 5.2, Stockholm, Sverige, [www.comsol.com](http://www.comsol.com).
- [43] D. Albinsson, S. Nilsson, T. J. Antosiewicz, V. P. Zhdanov, and C. Langhammer, Heterodimers for *in situ* plasmonic spectroscopy: Cu nanoparticle oxidation kinetics, Kirkendall effect, and compensation in the Arrhenius parameters, *J. Phys. Chem. C* **123**, 6284 (2019).
- [44] M. Mansour, L. Favergeon, and M. Pijolat, Kinetic modeling of low temperature oxidation of copper nanoparticles by  $\text{O}_2$ , *Thermochim. Acta* **570**, 41 (2013).
- [45] M. D. Susman, Y. Feldman, T. A. Bendikov, A. Vaskevich, and I. Rubinstein, Real-time plasmon spectroscopy study of the solid-state oxidation and Kirkendall void formation in copper nanoparticles, *Nanoscale* **9**, 12573 (2017).
- [46] M. Fanfoni and M. Tomellini, The Johnson-Mehl-Avrami-Kolmogorov model: A brief review, *Nuovo Cimento Della Soc. Ital. Di Fis. D* **20**, 1171 (1998).
- [47] J. C. Yang, D. Evan, and L. Tropa, From nucleation to coalescence of  $\text{Cu}_2\text{O}$  islands during *in situ* oxidation of Cu(001), *Appl. Phys. Lett.* **81**, 241 (2002).
- [48] G. Zhou and J. C. Yang, Initial oxidation kinetics of copper (1 1 0) film investigated by *in situ* UHV-TEM, *Surf. Sci.* **531**, 359 (2003).
- [49] Q. Zhu, L. Zou, G. Zhou, W. A. Saidi, and J. C. Yang, Early and transient stages of Cu oxidation: Atomistic insights from theoretical simulations and *in situ* experiments, *Surf. Sci.* **652**, 98 (2016).
- [50] K. P. Chen, V. P. Drachev, J. D. Borneman, A. V. Kildishev, and V. M. Shalaev, Drude relaxation rate in grained gold nanoantennas, *Nano Lett.* **10**, 916 (2010).
- [51] R. F. Egerton, *TEM specimens and images*, in *Physical Principles of Electron Microscopy* (Springer, New York, 2005), pp. 93–124.
- [52] Z. Yu, D. A. Muller, and J. Silcox, Study of strain fields at A-Si/c-Si interface, *J. Appl. Phys.* **95**, 3362 (2004).
- [53] T. Nilsson Pingel, M. Jørgensen, A. B. Yankovich, H. Grönbeck, and E. Olsson, Influence of atomic site-specific strain on catalytic activity of supported nanoparticles, *Nat. Commun.* **9**, 2722 (2018).
- [54] J. R. Sambles, Grain-boundary scattering and surface plasmon attenuation in noble metal films, *Solid State Commun.* **49**, 343 (1984).
- [55] M. Bosman, L. Zhang, H. Duan, S. F. Tan, C. A. Nijhuis, C. W. Qiu, and J. K. W. Yang, Encapsulated annealing: enhancing the plasmon quality factor in lithographically-defined nanostructures, *Sci. Rep.* **4**, 5537 (2014).
- [56] L. J. Tauzin, Y. Y. Cai, K. W. Smith, S. A. Hosseini Jebeli, U. Bhattacharjee, W. S. Chang, and S. Link, Exploring the relationship between plasmon damping and luminescence in lithographically prepared gold nanorods, *ACS Photonics* **5**, 3541 (2018).
- [57] J. C. Tinguely, I. Sow, C. Leiner, J. Grand, A. Hohenau, N. Felidj, J. Aubard, and J. R. Krenn, Gold nanoparticles for plasmonic biosensing: The role of metal crystallinity and nanoscale roughness, *Bionanoscience* **1**, 128 (2011).
- [58] E. Runge and E. K. U. Gross, Density-Functional Theory for Time-Dependent Systems, *Phys. Rev. Lett.* **52**, 997 (1984).
- [59] M. Petersilka, U. J. Gossmann, and E. K. U. Gross, Excitation Energies from Time-Dependent Density-Functional Theory, *Phys. Rev. Lett.* **76**, 1212 (1996).
- [60] V. M. Silkin, E. V. Chulkov, and P. M. Echenique, First-principles calculation of the electron inelastic mean free path in be metal, *Phys. Rev. B* **68**, 205106 (2003).
- [61] N. Troullier and J. L. Martins, Efficient pseudopotentials for plane-wave calculations, *Phys. Rev. B* **43**, 1993 (1991).
- [62] D. M. Ceperley and B. J. Alder, Ground State of the Electron Gas by a Stochastic Method, *Phys. Rev. Lett.* **45**, 566 (1980).

- [63] V. M. Silkin, E. V. Chulkov, I. Y. Sklyadneva, and V. E. Panin, Self-consistent calculation of the electron energy spectrum of aluminum, *Sov. Phys. J.* **27**, 762 (1984).
- [64] E. E. Krasovskii, A. N. Yaresko, and V. N. Antonov, Theoretical study of ultraviolet photoemission spectra of noble metals, *J. Electron Spectrosc. Relat. Phenom.* **68**, 157 (1994).
- [65] N. J. Simon, E. S. Drexler, and R. P. Reed, *Properties of Copper and Copper Alloys at Cryogenic Temperatures* (National Institute of Standards and Technology, Boulder, 1992).
- [66] S. Alekseeva, A. B. da S. Fanta, B. Iandolo, T. J. Antosiewicz, F. A. A. Nugroho, J. B. Wagner, A. Burrows, V. P. Zhdanov, and C. Langhammer, Grain boundary mediated hydriding phase transformations in individual polycrystalline metal nanoparticles, *Nat. Commun.* **8**, 1084 (2017).
- [67] K. M. McPeak, S. V. Jayanti, S. J. P. Kress, S. Meyer, S. Iotti, A. Rossinelli, and D. J. Norris, Plasmonic films can easily be better: Rules and recipes, *ACS Photonics* **2**, 326 (2015).
- [68] H. R. Philipp, Optical properties of silicon nitride, *J. Electrochem. Soc.* **120**, 295 (1973).
- [69] D. Tahir and S. Tougaard, Electronic and optical properties of Cu, CuO and Cu<sub>2</sub>O studied by electron spectroscopy, *J. Phys.: Condens. Matter* **24**, 175002 (2012).
- [70] K. P. Rice, R. R. Keller, and M. P. Stoykovich, Specimen-thickness effects on transmission Kikuchi patterns in the scanning electron microscope, *J. Microsc.* **254**, 129 (2014).
- [71] G. Kresse and J. Hafner, *Ab initio* molecular dynamics for liquid metals, *Phys. Rev. B* **47**, 558 (1993).
- [72] G. Kresse and J. Hafner, *Ab initio* molecular-dynamics simulation of the liquid-metalamorphous- semiconductor transition in germanium, *Phys. Rev. B* **49**, 14251 (1994).
- [73] G. Kresse and J. Furthmüller, Efficient iterative schemes for *ab initio* total-energy calculations using a plane-wave basis set, *Phys. Rev. B* **54**, 11169 (1996).
- [74] G. Kresse and J. Furthmüller, Efficiency of *ab-initio* total energy calculations for metals and semiconductors using a plane-wave basis set, *Comput. Mater. Sci.* **6**, 15 (1996).
- [75] P. E. Blöchl, Projector augmented-wave method, *Phys. Rev. B* **50**, 17953 (1994).
- [76] G. Kresse and D. Joubert, From ultrasoft pseudopotentials to the projector augmented-wave method, *Phys. Rev. B* **59**, 1758 (1999).
- [77] H. J. Monkhorst and J. D. Pack, Special points for brillouin-zone integrations, *Phys. Rev. B* **13**, 5188 (1976).
- [78] J. P. Perdew, K. Burke, and M. Ernzerhof, Generalized Gradient Approximation Made Simple, *Phys. Rev. Lett.* **77**, 3865 (1996).
- [79] L. Y. Isseroff and E. A. Carter, Importance of reference hamiltonians containing exact exchange for accurate one-shot GW calculations of Cu<sub>2</sub>O, *Phys. Rev. B* **85**, 235142 (2012).
- [80] G. Henkelman, B. P. Uberuaga, and H. Jónsson, Climbing image nudged elastic band method for finding saddle points and minimum energy paths, *J. Chem. Phys.* **113**, 9901 (2000).
- [81] C. G. Van De Walle and J. Neugebauer, First-principles calculations for defects and impurities: Applications to III-nitrides, *J. Appl. Phys.* **95**, 3851 (2004).